

Sparse Deconvolution Methods for Ultrasonic NDT

Application on TOFD and wall thickness measurements

**Florian Boßmann · Gerlind Plonka · Thomas
Peter · Oliver Nemitz · Till Schmitte**

Received: date / Accepted: date

Abstract In this work we present two sparse deconvolution methods for nondestructive testing. The first method is a special matching pursuit (MP) algorithm in order to deconvolve the mixed data (signal and noise), and thus to remove the unwanted noise. The second method is based on the approximate Prony method (APM). Both methods employ the sparsity assumption about the measured ultrasonic signal as prior knowledge. The MP algorithm is used to derive a sparse representation of the measured data by a deconvolution and subtraction scheme. An orthogonal variant of the algorithm (OMP) is presented as well. The APM technique also relies on the assumption that the desired signals are sparse linear combinations of (reflections of) the transmitted pulse. For blind deconvolution, where the transducer impulse response is unknown, we offer a general Gaussian echo model whose parameters can be iteratively adjusted to the real measurements. Several test results show that the methods work well even for high noise levels. Further, an outlook for possible applications of these deconvolution methods is given.

Keywords time of flight diffraction · matching pursuit · orthogonal matching pursuit · approximate Prony method · sparse blind deconvolution · parameter estimation · sparse representation

1 Introduction

Many ultrasonic testing applications are based on the estimation of the time of arrival (TOA), time of flight diffraction (TOFD) or the time difference of arrival (TDOA) of

F. Boßmann · G. Plonka · T. Peter
Institute for Numerical and Applied Mathematics, University of Göttingen, Lotzestraße 16-18, 37083
Göttingen, Germany
E-mail: {f.bossmann,plonka,t.peter}@math.uni-goettingen.de

O. Nemitz · T. Schmitte
Salzgitter Mannesmann Forschung GmbH, Ehinger Straße 200, 47259 Duisburg, Germany
E-mail: {o.nemitz,t.schmitte}@du.szmf.de

ultrasonic echoes. In order to analyze the received signals, one can usually suppose that the diffracted and backscattered echo from an isolated defect is a time-shifted, frequency-dissipated replica of the transmitted pulse with attenuated energy and inverted phase. In case of various flaw defects, the backscattered ultrasonic signal is a convolution of the modified pulse echo with the signal representing the reflection centers. Generally, we are faced with noisy measurements, where the noise is caused by reflections on microstructures of the tested material and electronic disturbances. It is therefore desirable to remove these effects from the recorded signal, i.e. to perform a deconvolution.

Most deconvolution techniques have been constructed for a time-invariant linear convolution model of the form

$$s(n) = x(n) * f(n) + v(n)$$

with a (sparse) time series $x(n)$ containing the relevant information on reflectivity, the transducer impulse response represented by the system $f(n)$, and a noise vector $v(n)$. Blind deconvolution methods are of special interest, where one has to estimate both, the reflectivity and the pulse from the same data, see [1,2]. Adaptive deconvolution methods are e.g. based on minimum entropy evaluation [3,4], on order statistics [5, 6], or on wavelet based regularization [7,8]. Similar methods can also be applied to B-scan images [9,10], where models with varying point spread functions have been considered.

However, the reflectivity will be sparse, and this is a powerful constraint that needs to be exploited for decorrelation. It can be directly integrated into the deconvolution model by considering

$$s(t) = \sum_{m=1}^M x(m)f(t - \tau_m) + v(t), \quad (1)$$

where we assume that the number M of non-zero coefficients is unknown but small, see e.g. [1,11]. In [1], a parametric model for the backscattered echo $f = f_{\theta}(t)$ is applied, where the parameter vectors $\theta = \theta_m$ are estimated using an expectation maximization (EM) algorithm or the space alternating generalized EM (SAGE) algorithm [12]. Unfortunately, there is no guaranty that these iterative algorithms converge to the wanted optimum. Therefore a good first guess for the parameters is crucial for the performance. Further, the EM algorithm converges very slowly [13]. The SAGE algorithm converges faster than EM under certain conditions but becomes unstable for low SNR [14]. Another drawback of the approach in [1] is that the number M of non-zero coefficients needs to be known beforehand.

In this paper, we want to apply a Gaussian echo function f_{θ} as introduced in [1] for simulating the modified transmitted pulse. Compared to [1], we simplify the model in (1) by assuming that the parameter vector θ determining the echo function f_{θ} does not depend on m . Hence, beside M , we have to determine the translations τ_m , the amplitudes $x(m)$ for $m = 1, \dots, M$ but only one parameter vector θ from the given data. Our tests with real data sets show that this simplified model is suitable for flaw detection in steel. Applying the model (1), we consider a general optimization

problem for blind deconvolution. The proposed numerical methods for solving this problem are very efficient.

For the deconvolution step we provide two methods; the first method is based on a (modified) matching pursuit (MP) algorithm [15, 16], the second uses the approximate Prony method (APM) [17]. In particular, we are able to compute the suitable number M of significant echoes in (1). For the iterative improvement of the model parameter vector θ , we employ an iterative Newton approach. The obtained deconvolution results are sparse vectors that contain only the most significant information of the original A-scans. In this way, a simple detection of flaw positions is possible, e.g. by employing a suitable classification method. Moreover, the proposed techniques allow for efficient storing of A-scans as well as for denoising. In the latter case, we just convolve the obtained sparse vectors with the ultrasonic pulse echo.

Recently, modified MP methods have already been applied for non-destructive testing [18–20], but not in relation with blind deconvolution. The interest in the MP method is due to its simple implementation and its numerical efficiency. The approximate Prony method has not been applied for sparse deconvolution before.

Experimental data discussed in this publication is obtained using standard ultrasonic non-destructive testing devices. Particularly, we consider the TOFD method for inspection of weld defects and the TOA method for measuring back wall deformations. For our special applications for inspection of weld defects using the TOFD method, the proposed methods can be further improved by comparison of neighboring A-scans in order to achieve higher robustness and precision.

Although we have restricted the numerical experiments to ultrasonic NDT of steel, the proposed deconvolution methods are also applicable to A-scans from other application fields as e.g. aluminum (cement) or biological measurements.

2 The model for signal representation

For representation of a received signal $s(t)$, we suppose that it can be obtained as a linear combination of time-shifted, energy-attenuated versions of the transmitted pulse function with inverted phase, where each shift is caused by an isolated flaw scattering the transmitted pulse. Usually, we have only a certain estimate of the transmitted pulse function. Using the approach in [1], we model the pulse echo by a real-valued Gabor function of the form

$$f_{\theta}(t) = K_{\theta} e^{-\alpha t^2} \cos(\omega t + \phi), \quad (2)$$

with the parameters $\theta = (\alpha, \omega, \phi)$. Here, α describes the bandwidth factor, ω is the center frequency, and ϕ the phase of the pulse echo. Because of its Gaussian shape envelope, this model is called Gaussian echo model. These parameters have intuitive meanings for the reflected pulse; the bandwidth factor α determines the bandwidth of the echo and hence the time duration of the echo in time domain. The frequency ω is governed by the transducer center frequency.

The normalization factor K_{θ} is taken such that $\|f_{\theta}\|_2 = 1$. More precisely, we obtain

$$K_{\theta}^{-2} = \|e^{-\alpha t^2} \cos(\omega t + \phi)\|_2^2 = \int_{-\infty}^{\infty} e^{-2\alpha t^2} \cos^2(\omega t + \phi) dt$$

$$= \frac{\sqrt{\pi}}{2\sqrt{2\alpha}}(1 + \cos(2\phi)e^{-\omega^2/8\alpha}), \quad (3)$$

where we have used that $\int_{-\infty}^{\infty} e^{-2\alpha t^2} \sin(2\omega t) dt = 0$ since the integrand is an odd function. In [1], the feasibility of this model has been demonstrated by a setup for a planar surface reflector using a steel sample, where the experimental echo is fitted by the Gaussian echo.

Our own experimental results also show that (2) is well suited for pulse echo approximation, see Figure 1. For given B-scans obtained by TOFD or by measuring back wall deformations, we use the following procedure to extract the pulse echo. In a first step, we compute the mean value of each row of the B-scan separately. In the obtained mean value vector (mean A-scan), we separate the back wall echo, normalize its maximal amplitude to 1 (see Figure 1, second column), and take this result as an approximation of the pulse echo for one scatterer. This procedure gives a good estimate for an A-scan that is obtained by a back wall echo only, since the material flaws are rare and yield signals with a small amplitude. The obtained pulse echoes can be well approximated by the Gaussian echo model in (2), see Figure 1, third column. The B-scans of TOFD data used in the first and second row in Figure 1 originate from two samples of a large-diameter pipe (outer diameter 1066 mm, wall thickness 23.3 mm). The corresponding complete TOFD B-scans are presented in Figures 10(a) and 11(a). In the third row, the B-scan of a back wall is used that originates from a sample of a steel pipe of outer diameter 244.5 mm and wall thickness 13.8 mm (see also Figure 12(a)). For a detailed technical description of the three B-scans we refer to Section 6.2. The approximation with the Gaussian echo model uses $\theta = (6.8486, 14.685, -2, 0836)$ in the first row, $\theta = (30.0, 28.039, 3.0867)$ in the second row, and $\theta = (45.0, 35.448, 1.5708)$ in the third row, where α and ω are given in $(MHz)^2$ and in MHz , respectively.

Observe that the approximated back wall echo already includes the change of pulse shape caused by frequency dependent attenuation in the material. Particularly, due to the angle of incidence of the transducer, the back wall echo is in fact a sum of pulse echoes with almost equal arrival times that cannot be separated into its original parts but is taken as one echo function.

We usually expect that there exists only a small number M of relevant scatterers corresponding to serious flaws in the material while microstructures in the material cause noise. Therefore, the backscattered signal can be approximated by a superposition of time-shifted pulse echoes

$$s(t) = \sum_{m=1}^M \tilde{a}(m) f_{\theta}(t - \tau_m) + v(t), \quad (4)$$

where the time shifts τ_m are related to the location of the relevant flaws, $\tilde{a}(m)$ are the amplitudes, and $v(t)$ denotes additive white Gaussian noise due to the measurement device. In Figure 2, we illustrate an example for a superposition of type (4) with $M = 5$ amplitudes.

In practice, the number M of relevant pulse reflections in (4) is unknown, but we may easily determine an upper bound depending on the application. Observe that

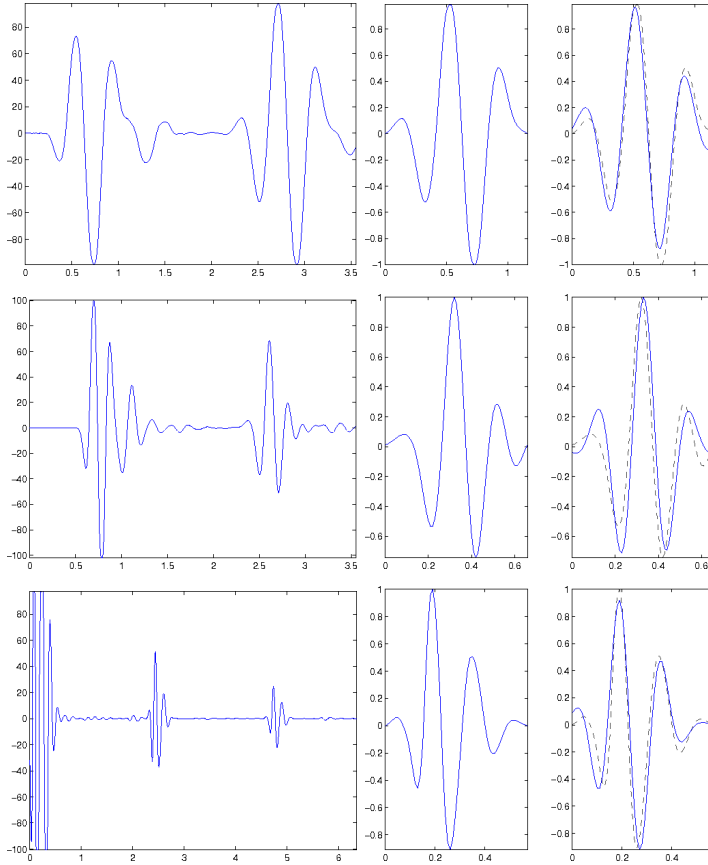


Fig. 1 Left: vector of mean values from real data (TOFD and back wall detection), middle: separated back wall echo, right: approximation by a Gabor function (2), for better comparison the separated back wall echo is presented by a dashed line; time in microseconds.

this model (4) is different from that in [1], since we assume here that all relevant reflections in the sum have the same parameter set θ , while only the amplitudes $\tilde{a}(m)$ and the time shifts τ_m change with m . This simplified model represents echoes from flaws or smooth surfaces with reasonable accuracy and provides good solutions for the practical problems at hand in this paper. Particularly, this simplification enables us to obtain fast algorithms for the estimation of all model parameters and to evaluate the number M of significant reflections during the computations. The changes in pulse echo shape due to the frequency dependent attenuation of the material are already (at least partially) covered by using the back wall echo approximation to determine a first guess for θ , see Figure 1. However, in case that one may switch to the more complex model of [1], which is needed for more complex shape echoes obtained e.g. for composite materials, the parameters obtained for the simplified model may serve as a very suitable first guess in the EM or the SAGE algorithm.

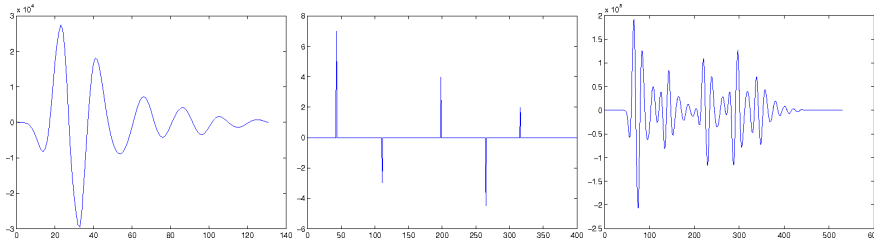


Fig. 2 Example for a pulse echo $f_{\theta}(t)$ (left), 5 amplitudes $\tilde{a}(m)$ (middle), and the superposition $s(t) = \sum_{m=1}^5 \tilde{a}(m) f_{\theta}(t - \tau_m)$.

We are now faced with the inverse problem of finding the relevant time-shifts τ_m and the corresponding amplitudes \tilde{a}_m as well as a suitable parameter vector θ from the given signal $s(t)$. Assuming that we have a first estimate of the parameter vector $\theta^{(0)} = (\alpha^{(0)}, \omega^{(0)}, \phi^{(0)})$, we would like to compute $\tilde{\mathbf{a}} = (\tilde{a}(1), \dots, \tilde{a}(M))^T \in \mathbb{R}^M$ and $\boldsymbol{\tau} = (\tau_1, \dots, \tau_M)^T \in \mathbb{R}^M$, and improve the pulse echoes simultaneously. Let s be the measured backscattered signal, and let F be a nonlinear operator that maps the parameter set $(\tilde{\mathbf{a}}, \boldsymbol{\tau}, \theta)$ to the function $\sum_{m=1}^M \tilde{a}(m) f_{\theta}(\cdot - \tau_m)$. Then, we aim to solve the optimization problem

$$\arg \min_{\tilde{\mathbf{a}}, \boldsymbol{\tau}, \theta} \|F(\tilde{\mathbf{a}}, \boldsymbol{\tau}, \theta) - s\|_2 \quad (5)$$

under the restriction that the number M of terms in $F(\tilde{\mathbf{a}}, \boldsymbol{\tau}, \theta)$ is as small as possible.

Some remarks about the noise are in order. In fact, we have to consider two different types of noise. On the one hand, there are unwanted reflections of the pulse echo in the A-scan caused by inhomogeneities in the material. On the other hand, we are faced with noise due to the measurement device. For the second type (called $v(t)$ in the model (4)) we can assume white Gaussian noise with expectation zero. Therefore it needs not to be considered in (5). The first type of noise, called microstructure noise, is more relevant and may be strong. It is contained in the sum (4) and enlarges the number M of components in the sum, and it will be suppressed in (5) by the restriction condition that the number M of terms in (4) is small. In fact, we need to assume here that microstructure echoes are smaller in amplitude than the flaw echoes, otherwise the deconvolution methods in Section 3 will not be able to separate them and noise may be wrongly taken as a significant flaw echo, see Section 6.

The optimization problem in (5) is very difficult to solve since the considered operator is nonlinear and not convex with respect to the parameters. The problem is even more delicate if the number of significant echoes M is not known. A usual approach to tackle such a complex problem is to separate it into subproblems that can be solved easier. If M is known beforehand and small, the EM algorithm (or a generalized version of it) can be employed to compute the maximum likelihood estimation (MLE), [1, 13, 14]. For that purpose, the function $s(t) = \sum_{m=1}^M \tilde{a}(m) f_{\theta}(t - \tau_m) + v(t)$ is separated into the (unknown) summands

$$x_m = \tilde{a}(m) f_{\theta_m}(t - \tau_m) + v_m(t) \quad m = 1, \dots, M$$

with $\sum_{m=1}^M v_m(t) = v(t)$. Supposed, that there are given the parameters $\tilde{a}^k(m)$, τ_m^k , θ_m^k from the k th iteration, one tries to improve the current expectation of x_m in the expectation step (E-step) by

$$\hat{x}_m^k = \tilde{a}^k(m) f_{\theta_m^k}(\cdot - \tau_m^k) + \frac{1}{M} \left(s - \sum_{m=1}^M \tilde{a}^k(m) f_{\theta_m^k}(\cdot - \tau_m^k) \right)$$

for $m = 1, \dots, M$ and solves the minimization problem in the M-step separately for each m ,

$$(\tilde{a}^{k+1}(m), \tau_m^{k+1}, \theta_m^{k+1}) = \arg \min_{\tilde{a}(m), \tau_m, \theta_m} \|\hat{x}_m^k - \tilde{a}(m) f_{\theta_m}(\cdot - \tau_m)\|^2.$$

Observe that the M subproblems considered in the EM algorithm are only coupled by the condition $s \approx \sum_{m=1}^M \tilde{a}^k(m) f_{\theta_m^k}(\cdot - \tau_m^k)$ in the expectation step, and this yields the very slow convergence of the EM algorithm. However, while the conditions that imply convergence to the global minimum of (5) can not be verified (see [13]), the method gives good parameter estimates, supposed that one starts with a suitable first guess.

Here we want to propose another separation method for the simplified model that enables us to compute also the unknown M .

Suppose that we have an initial guess $\theta^{(0)}$ for the choice of the pulse function that may be obtained experimentally from the data as above. In order to find a suitable solution of (5) we propose the following iterative method that consists of two steps in each iteration.

1. Solve the problem

$$(\tilde{\mathbf{a}}^{(k)}, \tau^{(k)}) := \arg \min_{\tilde{\mathbf{a}}, \tau} \|F(\tilde{\mathbf{a}}, \tau, \theta^{(k-1)}) - s\|_2 \quad (6)$$

under the restriction that the number M of terms in $F(\tilde{\mathbf{a}}, \tau, \theta^{(k-1)})$ is as small as possible. For that purpose, we propose the matching pursuit (MP) method in Section 3 or the approximate Prony method (APM) in Section 4.

2. Solve the minimization problem

$$\theta^{(k)} := \arg \min_{\theta} \|F(\tilde{\mathbf{a}}^{(k)}, \tau^{(k)}, \theta) - s\|_2 \quad (7)$$

using an iterative Newton-method represented in Section 5.

Regarding the applications, we are especially interested in ultrasonic testing of steel. Here, we use two different arrangements. In the first arrangement (TOFD inspection of weld seams) we use two probes, one transmitter and one receiver, see Figure 3. The transmitter produces a relatively wide beam spread to maximize the extent of the scan. The two probes are aligned geometrically on each side of the weld, and an A-scan is taken at sequential positions along the length of the seam. A typical A-scan usually detects

- the lateral signal which travels along the surface of the component and has shortest arrival time;

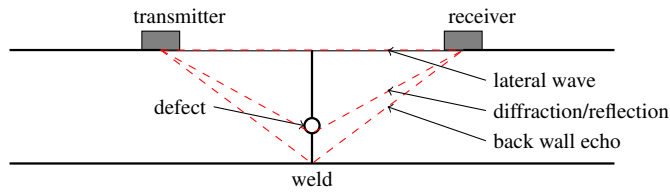


Fig. 3 TOFD probes arrangement for weld inspection.

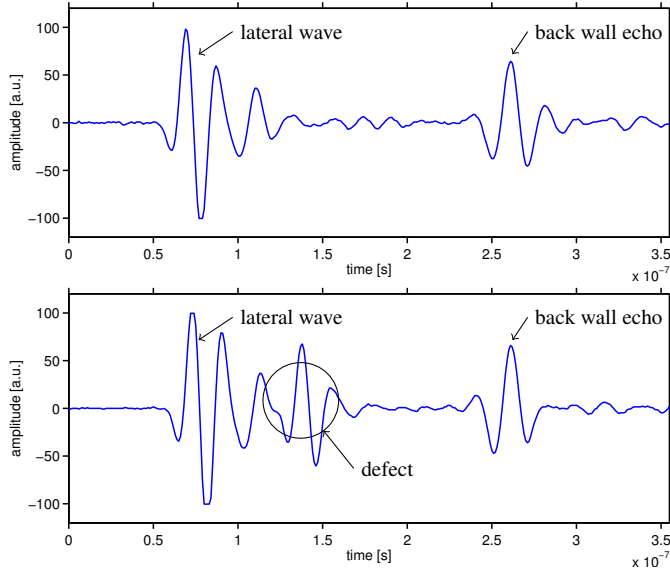


Fig. 4 Example of TOFD A-scans. Top: A-scan without a flaw; bottom: A-scan with a flaw. These A-scans are taken from the TOFD data in Figure 11.

- the back wall echo, which has longest transit time, see Figure 4.

In the second arrangement (inspection of back wall deformations), transmitter and receiver coincide and the beam is focussed to the back wall. In case of defects, also the corresponding signal reflection can be observed in the A-scan.

Observe that the proposed iteration method that separates the optimization of the arrival times and amplitudes from the optimization of bandwidth factor, center frequency and phase also gives no guaranty for global convergence. However, using the initial parameter vector $\theta^{(0)}$ obtained from approximating the back wall echo as given above, we usually obtain reasonable results for the parameters already by using just the first step of the proposed iteration (and keeping the $\theta = \theta^{(0)}$ just from the approximation).

3 Deconvolution based on greedy algorithms

We are especially interested in fast algorithms for detection of arrival times in the proposed models. Therefore, we propose first a matching pursuit approach that has been introduced in [15], see also [16] and references therein. It has been considered earlier in ultrasonic nondestructive testing; we refer to [18] as well as to modified versions as high resolution pursuit [19] and support matching pursuit [20]. In opposite to [18–20], we apply this idea firstly in connection with parameter estimation for the pulse model for blind deconvolution.

Generally, the matching pursuit algorithm works as follows. Let us assume that a given function s in a Hilbert space H can be well approximated by a linear combination of given functions b_j from a dictionary $\mathcal{D} = \{b_1, \dots, b_D\}$. In the first step, one iteratively seeks for the dictionary function b_j that correlates best with s . Then the same procedure is applied to the residuum $r_1 = s - \langle s, b_j \rangle b_j$ and so forth. In order to apply this idea to our model, we first need a suitable discretization. We suppose in this section that the parameter vector θ describing the pulse functions f_θ is given, such that we have to solve (6) for unknown τ and $\tilde{\mathbf{a}}$ and under the restriction that M is small. A procedure for iterative adjusting of the parameter vector θ will be presented in Section 5.

3.1 Discretization of the model

In practice, the received signal (A-scan) s is given as a vector of sampled signal values $\mathbf{s} = (s(n\Delta_t))_{n=0}^N$, where Δ_t denotes the sampling distance and $N + 1$ is the number of data.

Further, we can discretize the pulse echo f_θ with the same sampling distance Δ_t , i.e. let $\mathbf{f}_\theta = (f_\theta(\ell\Delta_t))_{\ell=-L}^L$ with $2L \ll N$, where we use only a finite number of function values, since f_θ decays rapidly. We assume that all relevant shifts of the impulse function $f_\theta(t)$ are completely recorded by the sampled data. Then a discretization of the received signal s can be modeled by

$$s(n\Delta_t) = \sum_{k=L}^{N-L} \tilde{a}(k) f_\theta((n-k)\Delta_t) + \nu(n\Delta_t), \quad n = 0, \dots, N, \quad (8)$$

where $\tilde{\mathbf{a}} = (\tilde{a}(k))_{k=L}^{N-L}$ denotes the vector of $K + 1$ (unknown) amplitudes, where $K := N - 2L$. A comparison of this representation of s with the sparse representation in (4) yields that we can suppose that only a small number $M \ll K + 1$ of coefficients in $\tilde{\mathbf{a}} = (\tilde{a}(k))_{k=L}^{N-L}$ has a modulus being significantly different from zero, and the significant components are assumed to have the indices $k_m \in \mathbb{Z}$ with $L \leq k_1 < \dots < k_M \leq N - L$. Hence, the relevant time-shifts τ_m in (4) are given by $\tau_m = k_m \Delta_t$.

We denote the coefficient matrix of the linear system in (8) by $\mathbf{F}_\theta = \mathbf{F}_{\theta, \Delta_t} = (f_\theta((n-k)\Delta_t))_{n=0, k=L}^{N, N-L}$ and can shortly write

$$\mathbf{F}_{\theta, \Delta_t} \tilde{\mathbf{a}} + \boldsymbol{\nu} = \mathbf{s}, \quad (9)$$

where $\boldsymbol{\nu} = (v(0), v(\Delta_t), \dots, v(N\Delta_t))^T$ is the Gaussian noise vector modeling the measurement errors while the structural errors occur as small components in $\tilde{\mathbf{a}}$. The matrix-vector representation reads

$$\begin{pmatrix} f_\theta(-L\Delta_t) & 0 & \dots & 0 \\ f_\theta((-L+1)\Delta_t) & f_\theta(-L\Delta_t) & & \vdots \\ f_\theta((-L+2)\Delta_t) & f_\theta((-L+1)\Delta_t) & & \\ \vdots & \vdots & \ddots & f_\theta(-L\Delta_t) \\ f_\theta(L\Delta_t) & & & f_\theta((-L+1)\Delta_t) \\ 0 & f_\theta(L\Delta_t) & & \\ \vdots & \ddots & \ddots & \vdots \\ 0 & \dots & 0 & f_\theta(L\Delta_t) \end{pmatrix} \tilde{\mathbf{a}} + \boldsymbol{\nu} = \mathbf{s}. \quad (10)$$

This linear system is overdetermined and needs to be solved approximately under the restriction that the coefficient vector $\tilde{\mathbf{a}}$ is sparse, i.e., contains only $M \ll K + 1$ elements. Using this discretization, we now look for a solution of the optimization problem

$$\min_{\tilde{\mathbf{a}}} \|\mathbf{F}_\theta \tilde{\mathbf{a}} - \mathbf{s}\|_2$$

under the restriction that the subnorm $M = \|\tilde{\mathbf{a}}\|_0$, i.e. the number of nonzero components in $\tilde{\mathbf{a}}$, is small. Here again, the relevant noise is suppressed by this additional restriction on the size of M and the white noise vector $\boldsymbol{\nu}$ with expectation zero needs not to be considered in the minimization problem.

3.2 Matching Pursuit

Considering the linear system $\mathbf{F}_\theta \tilde{\mathbf{a}} + \boldsymbol{\nu} = \mathbf{s}$, we denote the columns of the matrix \mathbf{F}_θ by $\mathbf{f}_0, \dots, \mathbf{f}_K$, where $K = N - 2L$. Here, $\{\mathbf{f}_0, \dots, \mathbf{f}_K\}$ is the dictionary for our MP method (in the Hilbert space \mathbb{R}^{N+1}). The system (9) can also be rewritten in the form

$$\mathbf{s} = \sum_{k=0}^K a(k) \mathbf{f}_k + \boldsymbol{\nu},$$

(where $a(k) := \tilde{a}(k+L)$) i.e., \mathbf{s} can be approximated by a linear combination of the columns \mathbf{f}_k . In a first step, we determine the index $k_1 \in \{0, \dots, K\}$ such that the column \mathbf{f}_{k_1} correlates most strongly with \mathbf{s} , i.e.

$$k_1 = \arg \max_{k=0, \dots, K} |\langle \mathbf{s}, \mathbf{f}_k \rangle|,$$

where $\langle \mathbf{s}, \mathbf{f}_k \rangle = \mathbf{s}^T \mathbf{f}_k$ is the standard scalar product of the two vectors \mathbf{s} and \mathbf{f}_k .

In the next step, we determine the coefficient $a(k_1)$ such that the Euklidean norm $\|\mathbf{s} - a(k_1) \cdot \mathbf{f}_{k_1}\|_2$ is minimal, i.e. $a(k_1) = \langle \mathbf{s}, \mathbf{f}_{k_1} \rangle / \|\mathbf{f}_{k_1}\|_2^2$, where $\|\mathbf{f}_{k_1}\|_2$ denotes the Euklidean norm of \mathbf{f}_{k_1} .

Now we consider the residuum $\mathbf{r}_1 = \mathbf{s} - a(k_1) \mathbf{f}_{k_1}$ and proceed again with the first step, where \mathbf{s} is replaced by \mathbf{r}_1 .

Starting with $\mathbf{r}_0 = \mathbf{s}$ and with $\mathbf{a} = \mathbf{0}$, the summarized algorithm works in the j -th iteration as follows:

1. Determine an optimal index k_j such that \mathbf{f}_{k_j} correlates most strongly with the residuum \mathbf{r}_{j-1} , i.e.

$$k_j = \arg \max_{k=0, \dots, K} |\langle \mathbf{r}_{j-1}, \mathbf{f}_k \rangle|.$$

2. Update the coefficient $a(k_j)$ to $a(k_j) + \langle \mathbf{r}_{j-1}, \mathbf{f}_{k_j} \rangle / \|\mathbf{f}_{k_j}\|_2^2$, where $\langle \mathbf{r}_{j-1}, \mathbf{f}_{k_j} \rangle / \|\mathbf{f}_{k_j}\|_2^2$ solves the problem $\min_x \|\mathbf{r}_{j-1} - x \mathbf{f}_{k_j}\|_2$.

Put $\mathbf{r}_j = \mathbf{r}_{j-1} - a(k_j) \mathbf{f}_{k_j}$.

As a stopping criterion, we shall apply the following procedure. We determine a priori an upper bound \tilde{M} for the number of coefficients in (4) and a suitable error bound $\varepsilon > 0$. Then the MP iteration is stopped after $j < \tilde{M}$ iterations if

$$\max_{k=0, \dots, K} |\langle \mathbf{r}_{j-1}, \mathbf{f}_k \rangle| / \|\mathbf{f}_k\|_2^2 < \varepsilon,$$

and at latest after \tilde{M} iterations. Using a sufficiently large upper bound \tilde{M} for the number of scatterers, the MP iteration will be stopped by the error bound criterion, and in this way we can compute the number M of relevant pulse echoes.

Let us shortly consider the numerical complexity of the MP method. For the first step of the algorithm we need to compute $K + 1 = N - 2L + 1$ scalar products, where the vectors \mathbf{f}_k have at most $2L + 1$ nonzero components. Hence we need $(2L + 1)(N - 2L + 1)$ multiplications, $2L(N - 2L + 1)$ additions as well as the comparisons to find a maximum of $N - 2L + 1$ numbers. Here we assume that $L \ll N$. For the second step we only need one division and one addition to compute $a(k_j)$, where we suppose that $\|\mathbf{f}_k\|_2^2 = \sum_{\ell=-L}^L f_\theta(\ell \Delta_t)^2$ is preliminarily computed with $2L + 1$ multiplications and $2L$ additions. Finally, \mathbf{r}_j is obtained with $2L + 1$ multiplications and $2L + 1$ additions. Hence the complete MP method with M iterations can be performed with $(4L + 1)NM - M(4L^2 - 2L - 5) + 4L + 2$ arithmetical operations, i.e., it is a $\mathcal{O}(N)$ algorithm and is therefore suitable for real time computations.

3.3 Orthogonal Matching Pursuit

The orthogonal matching pursuit algorithm works slightly different, see e.g. [16]. While the first step in each iteration stage is the same as before, the OMP replaces the update of only one coefficient $a(k_j)$ by a least square minimization in the second step, i.e. we use here

2. Update the coefficients $a(k_1), \dots, a(k_j)$ such that $\|\mathbf{s} - \sum_{i=1}^j a(k_i) \mathbf{f}_{k_i}\|_2$ is minimal and put $\mathbf{r}_j = \mathbf{s} - \sum_{i=1}^j a(k_i) \mathbf{f}_{k_i}$.

The least squares minimization problem $\min_{a(k_1), \dots, a(k_j)} \|\mathbf{s} - \sum_{i=1}^j a(k_i) \mathbf{f}_{k_i}\|_2$ leads to the linear system

$$(\langle \mathbf{f}_{k_i}, \mathbf{f}_{k_{i'}} \rangle)_{i, i'=1}^j (a(k_i))_{i=1}^j = (\langle \mathbf{s}, \mathbf{f}_{k_i} \rangle)_{i=1}^j. \quad (11)$$

In case of an orthonormal basis $\{\mathbf{f}_k : k = 0, \dots, K\}$, the coefficient matrix is the identity. But in our case, the shifts of the pulse function are not orthogonal. However, the number of considered vectors \mathbf{f}_i is smaller than M and the linear system (11) is of small dimension.

The OMP algorithm is more stable than the simple MP algorithm, since the update of all amplitudes in each iteration step ensures a better approximation of the signal s . Please note that this minimization does not effect the vectors \mathbf{f}_{k_i} themselves that are determined by the columns of $\mathbf{F}_{\theta, \Delta_t}$. However, since we are usually interested in a very small number of significant amplitudes, the MP algorithm already provides good results while being less time-consuming. Figure 5 in Section 6.1 shows the behavior of OMP for a single A-scan. Finally, we remark that the MP and the OMP algorithm of course also work for overlapping echoes, see Section 6.1. In this case the OMP is more robust.

4 Deconvolution based on the approximate Prony method

Now, we propose the approximate Prony method (APM), where we can obtain the number M of relevant scatterers during the algorithm. Furthermore, while the MP algorithm is restricted to a grid for finding the time-shifts $\tau_m = k_m \Delta_t$, the APM can detect arbitrarily distributed time-shifts. Let us consider again our sparsity model (4)

$$s(t) = \sum_{m=1}^M \tilde{a}(m) f_{\theta}(t - \tau_m) + v(t),$$

where we want to optimize over the time shifts $\boldsymbol{\tau} = (\tau_1, \dots, \tau_M)$, the amplitudes $\tilde{\mathbf{a}} = (\tilde{a}(1), \dots, \tilde{a}(M))$ and the pulse parameters θ , where M is unknown but small. We assume here that we have a suitable bound $\tilde{M} > M$ for the true number of relevant coefficients and can replace M by \tilde{M} in the above model. As in the last section, we first assume to have a good estimate for the parameter vector θ such that we can concentrate on the computation of $\boldsymbol{\tau}$ and $\tilde{\mathbf{a}}$ from the samples of s . For that purpose, we now adapt the approximate Prony method considered in [17] as follows.

Let the Fourier transform of a function $f \in L^1(\mathbb{R})$ be given by

$$\hat{f}(\xi) := \frac{1}{\sqrt{2\pi}} \int_{-\infty}^{\infty} f(t) e^{-i\xi t} dt.$$

Applying the Fourier transform to (4) (with M replaced by the bound $\tilde{M} > M$), we find

$$\hat{s}(\xi) = \left(\sum_{m=1}^{\tilde{M}} \tilde{a}(m) e^{-i\xi \tau_m} \right) \hat{f}_{\theta}(\xi) + \hat{v}(\xi).$$

In our case, the real-valued Gabor function $f_{\theta}(t) = K_{\theta} e^{-\alpha t^2} \cos(\omega t + \phi)$ is the real part of $g_{\theta}(t) = K_{\theta} e^{-\alpha t^2} e^{i(\omega t + \phi)} = K_{\theta} e^{i\phi} e^{-\alpha t^2} e^{i\omega t}$. Hence

$$\hat{f}_{\theta}(\xi) = \frac{1}{2} (\hat{g}_{\theta}(\xi) + \hat{\bar{g}}_{\theta}(\xi)) = \frac{K_{\theta}}{2\sqrt{2\alpha}} \left(e^{i\phi} e^{-(\omega - \xi)^2 / 4\alpha} + e^{-i\phi} e^{-(\omega + \xi)^2 / 4\alpha} \right). \quad (12)$$

Particularly, the function $\hat{f}_\theta(\xi)$ possesses only a zero at $\xi = 0$ if $\phi = \frac{(2\pi+1)\pi}{2}$ while $\hat{f}(\xi) \neq 0$ for all $\xi \neq 0$. Avoiding the case $\xi = 0$, we can hence write

$$\hat{h}(\xi) := \frac{\hat{s}(\xi)}{\hat{f}_\theta(\xi)} = \sum_{m=1}^{\tilde{M}} \tilde{a}(m) e^{-i\xi \tau_m} + \hat{\varepsilon}(\xi),$$

where the noise term $\hat{\varepsilon}(\xi) := \hat{v}(\xi)/\hat{f}_\theta(\xi)$ is assumed to be small.

For given samples $\hat{h}(k\Delta_\xi)$, (where Δ_ξ is a fixed sampling distance) we now aim to compute the frequencies $\tau_m \in \mathbb{R}_+$ and the corresponding amplitudes $\tilde{a}(m)$, for $m = 1, \dots, \tilde{M}$ separately using the following method. We consider the polynomial

$$\Lambda(z) = \prod_{m=1}^{\tilde{M}} (z - e^{-i\Delta_\xi \tau_m}) = \lambda_{\tilde{M}} z^{\tilde{M}} + \lambda_{\tilde{M}-1} z^{\tilde{M}-1} + \dots + \lambda_0$$

with $\lambda_{\tilde{M}} = 1$ that possesses the exponentials $e^{-i\Delta_\xi \tau_m}$ with the unknown time-shifts τ_m as zeros.

In a first step, we will determine the coefficients λ_k of the polynomial $\Lambda(z)$. We observe that for given sample values $\hat{h}((k+\ell)\Delta_\xi)$, $k = 0, 1, \dots$, and $\ell = 1, 2, \dots$, we have

$$\begin{aligned} \sum_{k=0}^{\tilde{M}} \lambda_k \hat{h}((k+\ell)\Delta_\xi) &= \sum_{k=0}^{\tilde{M}} \lambda_k \sum_{m=1}^{\tilde{M}} \tilde{a}(m) e^{-i\tau_m \Delta_\xi (k+\ell)} + \sum_{k=0}^{\tilde{M}} \lambda_k \hat{\varepsilon}((k+\ell)\Delta_\xi) \\ &\approx \sum_{m=1}^{\tilde{M}} \tilde{a}(m) e^{-i\tau_m \Delta_\xi \ell} \sum_{k=0}^{\tilde{M}} \lambda_k (e^{-i\tau_m \Delta_\xi})^k \\ &= \Lambda(e^{-i\tau_m \Delta_\xi}) \sum_{m=1}^{\tilde{M}} \tilde{a}(m) e^{-i\tau_m \Delta_\xi \ell} = 0, \end{aligned}$$

where we have assumed that the noise term $\sum_{k=0}^{\tilde{M}} \lambda_k \hat{\varepsilon}((k+\ell)\Delta_\xi)$ is negligibly small.

Using the above relation for $\ell = 1, 2, \dots, \tilde{M} + 1$, the unknown coefficients $\lambda_0, \dots, \lambda_{\tilde{M}-1}$ of $\Lambda(z)$ can be computed by finding an approximate zero eigenvector of the Hankel matrix

$$\mathbf{H} = \begin{pmatrix} \hat{h}(\Delta_\xi) & \hat{h}(2\Delta_\xi) & \dots & \hat{h}((\tilde{M}+1)\Delta_\xi) \\ \hat{h}(2\Delta_\xi) & \hat{h}(3\Delta_\xi) & & \hat{h}((\tilde{M}+2)\Delta_\xi) \\ \vdots & & & \vdots \\ \hat{h}((\tilde{M}+1)\Delta_\xi) & \hat{h}((\tilde{M}+2)\Delta_\xi) & \dots & \hat{h}((2\tilde{M}+1)\Delta_\xi) \end{pmatrix}.$$

We can now obtain the true number $M < \tilde{M}$ of suitable terms in the model (4) by a rank estimation of \mathbf{H} , since the rank of the matrix \mathbf{H} in the noiseless case coincides with the number M of suitable terms, see [17]. We apply the above eigenvalue problem to a Hankel matrix \mathbf{H} of size $(\tilde{M}+1) \times (\tilde{M}+1)$, i.e., we compute an approximate zero eigenvector of \mathbf{H} . This eigenvector contains the coefficients λ_k that are used to form the polynomial $\Lambda(z)$. We evaluate the corresponding zeros of the polynomial $\Lambda(z)$. The zeros of Λ that are relevant to us, are of the form $e^{-i\tau_m \Delta_\xi}$ and

lie (approximately) on the unit circle, such that we are able to determine the time shifts τ_m , $m = 1, \dots, M$. As shown in [17], each zero eigenvector of \mathbf{H} will yield the same relevant zeros $e^{-i\tau_m\Delta_\xi}$.

In the second part of the procedure, we can compute the amplitudes \tilde{a}_m as least square solution of the overdetermined linear system

$$\sum_{m=1}^M \tilde{a}_m f_\theta(\ell\Delta_t - \tau_m) = s(\ell\Delta_t), \quad \ell = 0, \dots, N,$$

thereby neglecting the noise function $v(t)$.

For application of the first step of above procedure, we need to evaluate the Fourier transform $\hat{h} = \hat{s}/\hat{f}_\theta$ at suitable values $k\Delta_\xi$. For this purpose we employ the fast Fourier transform as follows. Assume that we have given the sampled values of the backscattered signal $\mathbf{s} = (s(\ell\Delta_t))_{\ell=0}^N$. Using linear splines, s can be approximated by the sum

$$\tilde{s}(t) = \sum_{\ell=0}^N s(\ell\Delta_t) N_2(t - \ell\Delta_t),$$

where the B-spline N_2 has the support $[-(\Delta_t)^{-1}, (\Delta_t)^{-1}]$ and is given by $N_2(t) = (1 - \Delta_t|t|)$ for $t \in [-(\Delta_t)^{-1}, (\Delta_t)^{-1}]$. Then Fourier transform yields

$$\hat{\tilde{s}}(\xi) = \left(\sum_{\ell=0}^N s(\ell\Delta_t) e^{-i\xi\Delta_t\ell} \right) \hat{N}_2(\xi).$$

With $\hat{N}_2(\xi) = \frac{1}{\sqrt{2\pi}} \frac{1}{\Delta_t} \text{sinc}\left(\frac{\xi}{2\Delta_t}\right)^2$ and with the function $\hat{f}_\theta(\xi)$ that is explicitly given in (12), we obtain the approximate values

$$\hat{h}\left(\frac{2\pi k}{\Delta_t}\right) = \hat{h}(k\Delta_\xi) = \frac{\hat{\tilde{s}}(k\Delta_\xi)}{\hat{f}_\theta(k\Delta_\xi)},$$

where $\Delta_\xi := \frac{2\pi}{\Delta_t}$, $k = 0, \dots, N$, and where

$$\sum_{\ell=0}^N s(\ell\Delta_t) e^{-i\xi_k\Delta_t\ell}, \quad k = 0, \dots, N$$

is computed for $\xi_k = \frac{2\pi k}{\Delta_t}$ by the fast Fourier transform.

Remarks.

1. Compared with the MP method, the APM has the advantage that we are able to compute the time shifts τ_m exactly independently from the sampling grid with sampling size Δ_t . However, due to the needed Fourier transform, APM is computationally more expensive than the MP method. Although, APM has been established for noisy data measurements in [17], it is more sensitive to noise than the MP method.

2. The APM method is able to find relevant time-shifts τ_m with a small separation distance, i.e. it works also for overlapping pulse echoes, see Section 6.1. The separation distance influences the numerical stability of the algorithm. It can be chosen smaller if the number of data N is large (see [17]).

3. The MP (OMP) method and the APM method are fundamentally different with respect to their underlying ideas as well as to their numerical effort. The MP method is a greedy method, i.e. it will find the most significant amplitudes just by comparison of correlations of the shifted pulse echo with the measured data. While this method is very simple and efficient, it can fail for all further iterations if once a wrong shift is taken (possibly caused by strong noise). The number M of relevant scatters is found by using an initial bound for \tilde{M} and by observing the size of the remainder if the found significant pulse echoes are subtracted from the data. The AMP method is much smarter. It separates the search of arrival times from the determination of the corresponding amplitudes by transferring the model to the frequency domain. Unfortunately, the Fourier transform can enforce the error such that this method is more sensitive to low SNR values.

5 Optimization of the parameters

In the preceding sections we have assumed that a reliable estimate of the parameter vector θ determining the pulse echo is given. In Section 2, we have proposed an alternating minimization procedure for the stepwise improvement of the pulse echo parameters during the computation process.

Having solved the optimization problem (6) for small M using either the matching pursuit algorithm or the approximate Prony method, we shall now consider the second minimization problem (7) for adjusting the parameter vector θ . For that purpose we want to employ the iterative Newton method. Consider now the minimization problem

$$\theta^{(k)} := \arg \min_{\theta} \|F(\tilde{\mathbf{a}}^{(k)}, \boldsymbol{\tau}^{(k)}, \theta) - s\|_2.$$

A linearization of the operator around an initial guess $\theta^{(k-1)}$ yields

$$F(\tilde{\mathbf{a}}^{(k)}, \boldsymbol{\tau}^{(k)}, \theta^{(k-1)} + d\theta) \approx D_{\theta}F(\tilde{\mathbf{a}}^{(k)}, \boldsymbol{\tau}^{(k)}, \theta^{(k-1)})d\theta + F(\tilde{\mathbf{a}}^{(k)}, \boldsymbol{\tau}^{(k)}, \theta^{(k-1)}).$$

Here, $D_{\theta}F(\tilde{\mathbf{a}}^{(k)}, \boldsymbol{\tau}^{(k)}, \theta^{(k-1)})$ denotes the Jacobian of F at $\theta^{(k-1)}$, i.e.,

$$D_{\theta}F(\tilde{\mathbf{a}}^{(k)}, \boldsymbol{\tau}^{(k)}, \theta^{(k-1)}) = \left(\frac{\partial F(\tilde{\mathbf{a}}^{(k)}, \boldsymbol{\tau}^{(k)}, \theta^{(k-1)})}{\partial \alpha}, \frac{\partial F(\tilde{\mathbf{a}}^{(k)}, \boldsymbol{\tau}^{(k)}, \theta^{(k-1)})}{\partial \omega}, \frac{\partial F(\tilde{\mathbf{a}}^{(k)}, \boldsymbol{\tau}^{(k)}, \theta^{(k-1)})}{\partial \phi} \right).$$

Hence, the update vector $d\theta = (d\alpha, d\omega, d\phi)^T$ is obtained from the equation

$$D_{\theta}F(\tilde{\mathbf{a}}^{(k)}, \boldsymbol{\tau}^{(k)}, \theta^{(k-1)})d\theta + F(\tilde{\mathbf{a}}^{(k)}, \boldsymbol{\tau}^{(k)}, \theta^{(k-1)}) = s$$

and can be evaluated at the known samples $k\Delta_r$. This leads to a least squares problem which can be directly solved since the corresponding coefficient matrix has only three dimensions. In this way, we obtain the new update $\theta_1^{(k-1)} := \theta^{(k-1)} + d\theta$. One may proceed with the Newton iteration to obtain the updates $\theta_2^{(k-1)}, \theta_3^{(k-1)}, \dots$. After r Newton steps, where r that can be just fixed or can depend on some suitable error criterion, one obtains the new estimate $\theta^{(k)} = \theta_r^{(k-1)}$.

Unfortunately, because of the complicated normalization factor K_θ in (3), the vector $D_\theta F(\tilde{\mathbf{a}}^{(k)}, \tau^{(k)}, \theta^{(k-1)})$ can not be easily computed analytically. Therefore, we consider an analytical representation of

$$D_\theta \left(\frac{1}{K_\theta} F(\tilde{\mathbf{a}}, \tau, \theta) \right) = D_\theta \left(\sum_{m=1}^M \tilde{a}(m) e^{-\alpha(t-\tau_m)^2} \cos(\omega(t-\tau_m) + \phi) \right)$$

and obtain for $\theta = (\alpha, \omega, \phi)^T$,

$$D_\theta \left(\frac{1}{K_\theta} F(\tilde{\mathbf{a}}, \tau, \theta) \right) = \begin{pmatrix} - \sum_{m=1}^M \tilde{a}(m)(t-\tau_m)^2 e^{-\alpha(t-\tau_m)^2} \cos(\omega(t-\tau_m) + \phi) \\ - \sum_{m=1}^M \tilde{a}(m)(t-\tau_m) e^{-\alpha(t-\tau_m)^2} \sin(\omega(t-\tau_m) + \phi) \\ - \sum_{m=1}^M \tilde{a}(m) e^{-\alpha(t-\tau_m)^2} \sin(\omega(t-\tau_m) + \phi) \end{pmatrix}^T.$$

However, a change of the parameter vector θ implies a possibly considerable change of the norm K_θ^{-1} of the pulse function f_θ . A disregard of the normalization factor K_θ thus leads to a highly unstable method since the amplitudes in $\tilde{\mathbf{a}}$ are optimized with respect to the Euklidean norm of \mathbf{f}_θ . In order to counter this problem we are updating not only θ in each Newton step but also the amplitudes $\tilde{\mathbf{a}}$. In this way the amplitudes in $\tilde{\mathbf{a}}$ are adjusted to the changing wave norm. Therefore, we employ

$$D_{\theta, \tilde{\mathbf{a}}} \left(\frac{1}{K_\theta} F(\tilde{\mathbf{a}}, \tau, \theta) \right) = \begin{pmatrix} - \sum_{m=1}^M \tilde{a}(m)(t-\tau_m)^2 e^{-\alpha(t-\tau_m)^2} \cos(\omega(t-\tau_m) + \phi) \\ - \sum_{m=1}^M \tilde{a}(m)(t-\tau_m) e^{-\alpha(t-\tau_m)^2} \sin(\omega(t-\tau_m) + \phi) \\ - \sum_{m=1}^M \tilde{a}(m) e^{-\alpha(t-\tau_m)^2} \sin(\omega(t-\tau_m) + \phi) \\ e^{-\alpha(t-\tau_1)^2} \cos(\omega(t-\tau_1) + \phi) \\ \vdots \\ e^{-\alpha(t-\tau_M)^2} \cos(\omega(t-\tau_M) + \phi) \end{pmatrix}^T$$

in the iterative Newton method and update not only the parameter vector θ but also the coefficient vector $\tilde{\mathbf{a}}$ in our model (4). Our numerical results in Section 6.3 show the fast convergence of the iterative Newton method after only a few iteration steps.

For the numerical application of this procedure for parameter optimization we refer to Section 6.3.

6 Test results

We have tested the proposed procedures using simulated data as well as real data, particularly TOFD data of weld defects and TOA data of back wall deformations.

6.1 Simulated Data

In a first test, we want to show the performance of the OMP-method and the APM method to recover arrival times and amplitudes of a sum of four interfering echoes with different SNR. For that purpose, we consider two different scenarios. In the first scenario we have four interfering echoes being obtained by four shifts of the Gabor function f_θ with parameters $\alpha = 50(\text{MHz})^2$, $\omega = 25.1327\text{MHz}$ and $\phi = 0.52$ microseconds. The resolution is 10ns . Particularly, we study the behavior of the two deconvolution methods if one arrival time comes close to another in case of almost no noise (SNR of about 45.00). The four overlapping echoes considered in Table 1 are illustrated in Figure 5, top. In particular, one can observe that for approaching arrival times x and 7.20 with $7.15 \leq x < 7.20$ it is really difficult to recognize x and 7.20 as two different arrival times. For APM, the computed arrival times are rounded corresponding to the resolution. The obtained results, summarized in Table 1, show that the two proposed algorithms are suited also for recovering interfering echoes. In this (almost noiseless) case the APM is more stable than OMP when the arrival times of two echoes approach. If the echoes are too close, then OMP can not longer distinguish between them and takes it as one echo, where the amplitudes are added. For approaching arrival times with $7.15 \leq x < 7.20$, the OMP finds only one arrival times while the APM method recognizes two, where for a difference of 0.01 microseconds the corresponding amplitudes are not longer correctly attributed.

In the second scenario, we consider four shifts of the Gabor function f_θ with parameters $\alpha = 20(\text{MHz})^2$, $\omega = 50.2634\text{MHz}$ and $\phi = 0.52$ microseconds. We study the behavior of the deconvolution methods for changing low SNR, see Table 2. The corresponding noisy echo functions are illustrated in Figure 5, bottom. In particular, we observe that the two algorithms correctly estimate the four arrival times even in case of strong noise, while the obtained amplitudes are not exact. We remark that the MP algorithm works only slightly worse than OMP in the two experiments and is in fact as good as OMP for high noise levels.

Considering the data, there are mainly two components of noise: a) microstructure noise, produced by multiple reflections and inhomogeneous material, and b) electronic noise, fed from cables, amplifiers etc., which acts like a bandpass filter. The first can be considered as Gaussian noise in the coefficient vector $\tilde{\mathbf{a}}$, which results in colored noise after convolution with the wave. Hence, to test the algorithms with different noise levels and different wave forms we have modeled a back wall deformation as follows.

We have used the data in Figure 6 that originates from the measurement of a real back wall deformation in a steel pipe that has been extended by zero outside its support. Then, Gaussian noise with different variances (0.001, 0.01 and 0.025) has been added to the back wall data before convolving each column with a Gabor function of the form (2). We want to illustrate that the proposed deconvolution methods perform well for different Gabor functions. The simulated B-scans in the first row of Figure 8 are obtained using the convolution with the Gabor function with $\theta = (\alpha, \omega, \phi) = (20, 10, 0)$, where the bandwidth factor α is given in $(\text{MHz})^2$, and the center frequency ω in MHz . Analogously, the B-scans in the first row of Figure 9 are obtained by convolution of the noisy geometric model with a Gabor function

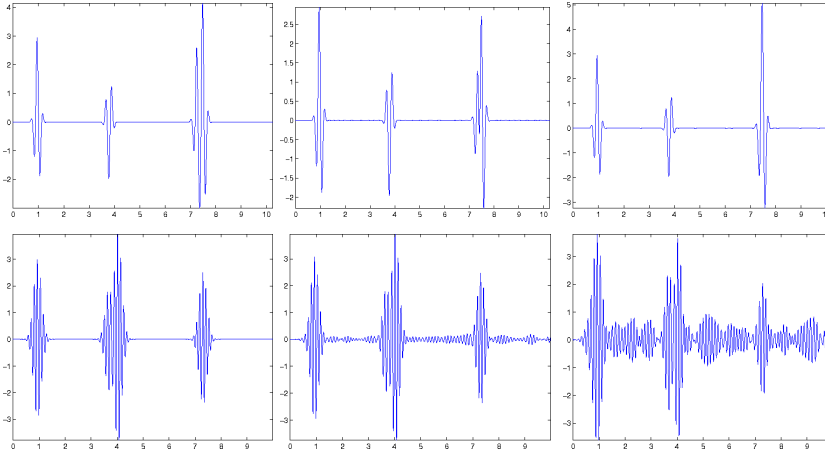


Fig. 5 Top: Four interfering echoes of the Gabor function f_θ with $\theta = (50(MHz)^2, 25.1327 MHz, 0.52\mu s)$ (almost noiseless case) with amplitudes and arrival times as given in Table 1 for $x = 6.96$ (left), $x = 7.07$ (middle) and $x = 7.15$ (right); Bottom: Four interfering echoes of the Gabor function f_θ with $\theta = (20(MHz)^2, 50.2634 MHz, 0.52\mu s)$ with amplitudes and arrival times as given in Table 2, without noise (left), with SNR of 19.34 (middle) and with SNR of 4.75 (right); time in microseconds.

actual parameters	arrival times (μs)				amplitudes			
	0.50	3.40	x	7.20	3.0	-2.0	2.5	4.0
time x	arrival times (μs) obtained by OMP				amplitudes obtained by OMP			
6.96	0.50	3.40	6.96	7.20	3.0028	-1.9937	2.5001	3.9988
7.07	0.50	3.40	6.95	7.21	3.0023	-2.0012	-1.3483	2.4355
7.15	0.50	3.40	7.18		2.9950	-1.9958	5.1517	
7.18	0.50	3.40	7.19		3.0030	-1.9950	6.2750	
7.19	0.50	3.40	7.20		2.9996	-2.0000	6.3707	
time x	arrival times (μs) obtained by APM				amplitudes obtained by APM			
6.96	0.50	3.40	6.96	7.20	2.9998	-1.9955	2.5013	3.9999
7.07	0.50	3.40	7.07	7.20	3.0007	-2.0023	2.5008	4.0031
7.15	0.50	3.40	7.15	7.20	3.0048	-1.9918	2.5027	4.0220
7.18	0.50	3.40	7.18	7.20	3.0014	-1.9979	2.1900	4.3127
7.19	0.50	3.40	7.20	7.21	3.0006	-1.9994	6.0532	0.4065

Table 1. Parameter estimation results for four interfering echoes when one arrival time gets close to another. The SNR of the interfering echoes is about 45.

with $\theta = (7.5, 10, \pi/2)$. The two different Gabor functions are illustrated in Figure 7. Observe that here noise simulates microstructure noise produced by inhomogeneities in the material since the noise has been added before the convolution with the pulse function.

In the second and third rows of Figures 8 – 9, we illustrate the behavior of the proposed MP resp. OMP algorithm. The reconstructed back wall echo time yields the wall thickness of the modeled tube correctly up to the discretization error. In the second row of Figure 8, we present the amplitudes of significant reflections of

actual parameters	arrival times (μs)				amplitudes				estimation SNR
	0.50	3.40	3.75	7.20	3.0	-2.0	4.0	2.5	
SNR	arrival times (μs) obtained by OMP				amplitudes obtained by OMP				
19.34	0.50	3.40	3.75	7.20	3.1000	-1.9727	3.9863	2.4562	34.22
13.10	0.50	3.40	3.75	7.20	3.1071	-1.9352	3.9093	2.4312	30.88
8.15	0.50	3.40	3.75	7.20	3.1085	-1.7118	3.9806	2.4363	25.37
4.75	0.50	3.40	3.75	7.19	4.0206	-2.5048	3.4768	1.9641	10.33
SNR	arrival times (μs) obtained by APM				amplitudes obtained by APM				
19.34	0.50	3.40	3.75	7.20	3.1107	-2.0841	3.9907	2.5646	28.85
13.10	0.50	3.40	3.75	7.20	3.0815	-2.0384	3.9552	2.5659	20.34
8.15	0.50	3.40	3.75	7.20	2.9960	-2.4391	4.3420	2.4048	18.13
4.75	0.50	3.39	3.75	7.20	3.7694	-2.8166	3.2185	2.2643	10.30

Table 2. Parameter estimation results for four interfering echoes with different SNR. For OMP the parameter $\varepsilon = 1.25$ is taken and the upper bound for arrival times is 5.

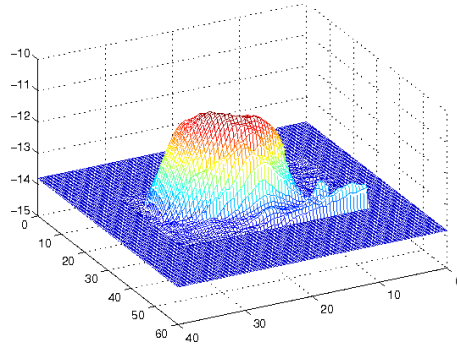


Fig. 6 3D illustration of the back wall deformation used in the simulations.

the pulse function computed with the matching pursuit (MP) method. In this case a nearly nonnegative Gabor wave is used as pulse function. The MP method has been used with at most $\tilde{M} = 5$ iterations and with $\varepsilon = 1.0$ in the first, $\varepsilon = 1.75$ in the second, and $\varepsilon = 1.5$ in the third column. Applying again a convolution to the obtained sparse A-scan vectors, we find a suitable approximation of the original B-scan (see third row in Figure 8). This sparse approximation efficiently denoises the original B-scan. The same experiment is performed with the APM proposed in Section 4. The fourth row of Figure 8 illustrates the amplitudes of significant reflections of the pulse function computed with the approximate Prony method. Here the number of significant amplitudes is found during the algorithm and it swings between 1 and 8 with an average of 1.65. Applying a convolution to the sparse A-scans we obtain the approximation presented in the last row of Figure 8.

Figure 9 shows the denoising results taking an antisymmetric Gabor wave as pulse echo and using OMP and APM. The OMP method is used here with $\tilde{M} = 5$ and with $\varepsilon = 1.0; 1.25; 1.5$ in the rows 1,2,3. The advantage of the APM is the ability to detect the significant translations without an underlying grid. In order to present these data in

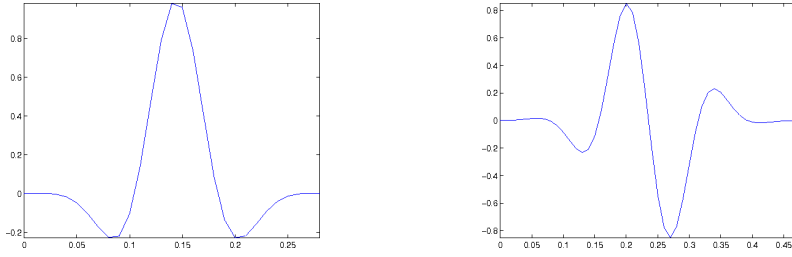


Fig. 7 Gabor pulse functions used for simulations of B-scans in Figures 8-9. Left: even Gabor function, right: odd Gabor function.

Figure	noise variance	SNR	MP/OMP		APM	
			mean M	compression rate	mean M	compression rate
Figure 8	0.001	16.30	1.2000	0.0043	1.6348	0.0059
	0.010	6.50	1.0087	0.0036	1.4609	0.0052
	0.025	2.52	1.8696	0.0067	2.0087	0.0072
Figure 9	0.001	18.25	1.3304	0.0045	1.6696	0.0056
	0.010	8.42	1.3130	0.0044	1.2348	0.0041
	0.025	4.38	1.5130	0.0052	1.8783	0.0063

Table 3. Comparison of the found mean number M of significant coefficients in each row for different noise levels, and the corresponding compression rates, see also Figures 8 and 9.

the the figures (fourth row in Figures 8 – 9), we have considered a traverse through the obtained amplitudes (approximation with a linear B-spline) instead of rounding the the found significant translations to the grid points. Therefore the obtained significant amplitudes are slightly different for the MP method and APM.

Besides the correct estimation of the arrival times found by the two deconvolution algorithms in the above experiment, we obtain a sparse approximation of the B-scans in terms of a small number of significant coefficients representing the relevant information. The number of significant coefficients found by MP/OMP resp. APM is presented in Table 3. Figures 8 and 9 show that it is possible to reconstruct the B-scan using only these significant coefficients. Observing that the B-scans in Figures 8 and 9 have 115 columns and 279 resp. 298 rows, we obtain compression rates of as given in Table 3.

We observe, that the MP and the OMP give reasonable results even for highly noisy data. The APM works accurately for the low-level noise case. The reason for that behavior is, that MP/OMP are rather robust algorithms whereas the APM is slightly less numerically stable for high noise levels. Thus the MP/OMP methods are more suitable for a fast determination of material defects while the APM is able to identify clustered defects in the low-level noise case, and may be especially appropriate for determining the more exact structure of a defect, after knowing where that defect is located. This problem will be considered further in the future.

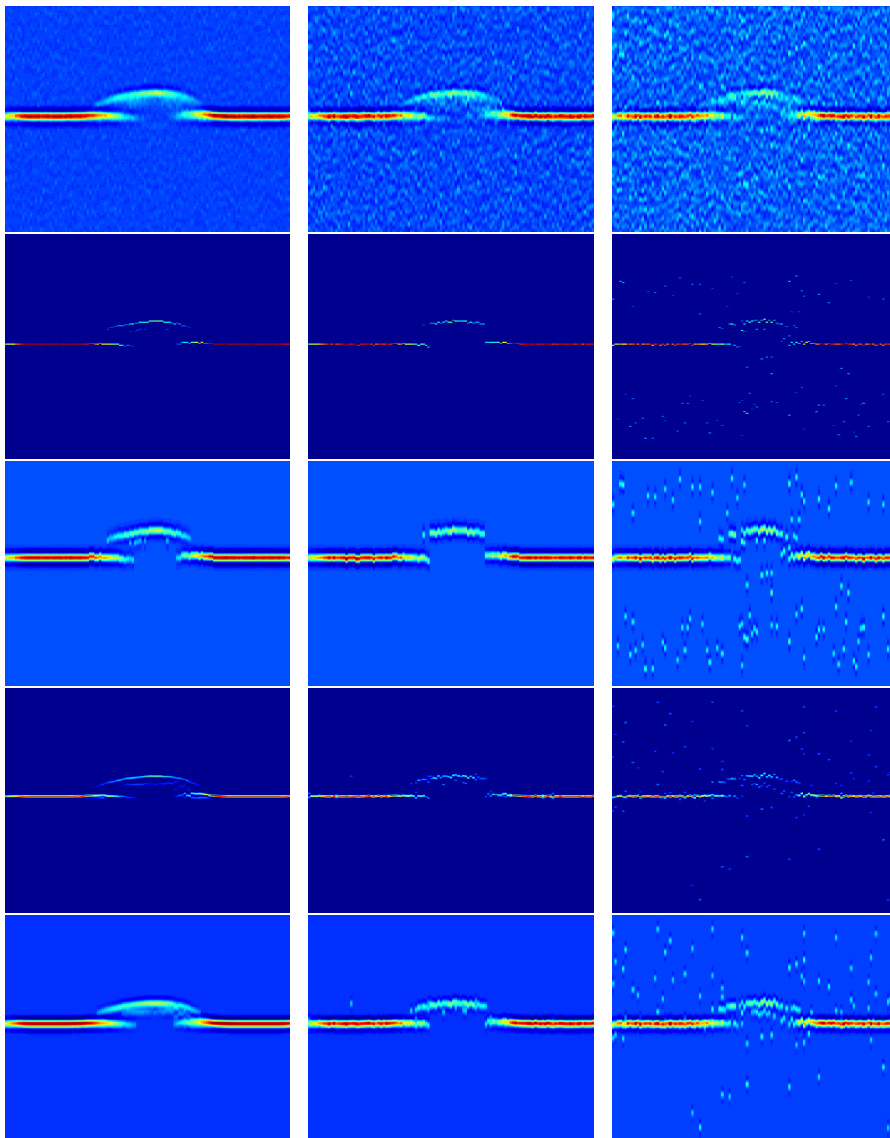


Fig. 8 Top: simulated back wall echo with different noise levels and nearly nonnegative Gabor wave, noise levels from left to right (Gaussian variance): 0.001, 0.01, 0.025; second row: obtained significant amplitudes after deconvolution with MP; third row: back wall reconstruction using only the significant amplitudes found by MP; fourth row: obtained significant amplitudes using APM; last row: back wall reconstruction using only the significant amplitudes found by APM.

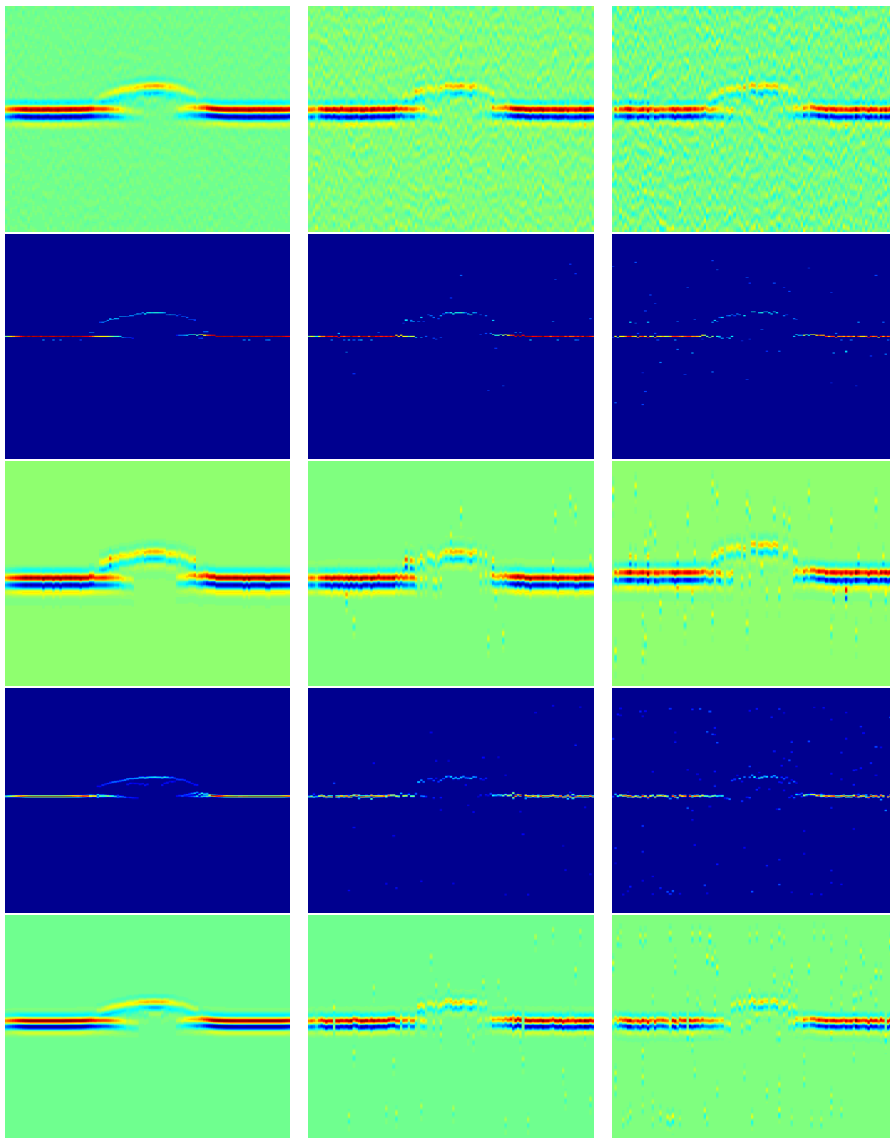


Fig. 9 Top: modeled back wall echo with different noise levels and antisymmetric Gabor wave, noise levels from left to right (Gaussian variance): 0.001, 0.01, 0.025; second row: obtained significant amplitudes after deconvolution with OMP; third row: back wall reconstruction using only the significant amplitudes found by OMP; fourth row: obtained significant amplitudes using APM; last row: back wall reconstruction using only the significant amplitudes found by APM.

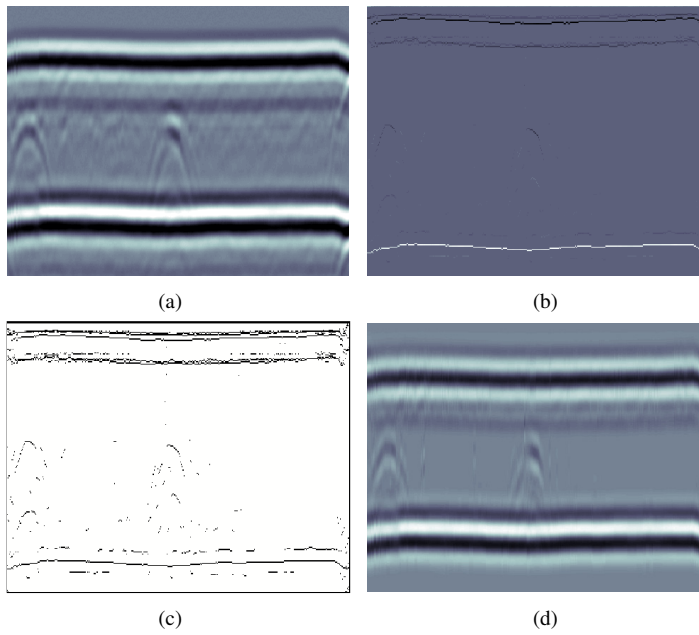


Fig. 10 (a): Original TOFD data; (b): approximative solution of $\bar{\mathbf{a}}$ with MP method in Section 3.2; (c): nonzero elements of the solution; (d): approximation of $\mathbf{s} \approx \mathbf{F} \cdot \bar{\mathbf{a}}$.

6.2 Real Data

Finally, we study the results of the deconvolution methods for real TOFD data and for back wall echoes.

The original TOFD data in Figure 10(a), and in Figure 11(a) has been obtained from a sample of a large-diameter pipe (outer diameter 1066 mm, wall thickness 23.3 mm). In Figure 10(a), the weld seam has been tested with a TOFD system (Olympus Omniscan iX) with a 5 MHz transducer, 6 mm diameter (Olympus C543-SM). In Figure 11(a), a 10 MHz transducer, 6 mm diameter (Olympus C563-SM) with the same system has been used. Both transducers were applied with a wedge with 70° angle of incidence. The flaws in Figure 10(a) are pores, while Figure 11(a) shows a lack of fusion at the end of the pipe, where the last part of the weld seam has been ground. Both B-scans are measured with a sampling rate of 100 MHz and an 8-bit resolution. The resolution in scan direction is 0.5 mm.

For TOFD signals the lateral signal as well as the back wall echo have generally significantly larger amplitudes than the signals indicating defects. In order to obtain the essential signals indicating weld deformations, we add suitable weights that can be chosen a priori using knowledge about the thickness of the tube and an estimate about positions of lateral signal and back wall echo in the A-scan. Since the ultrasonic wave send out by the emitter is not given, we estimate it from the given data in order to find a first approximation of the pulse echo of the form (2). This is done as given in Section 2, see Figure 1.

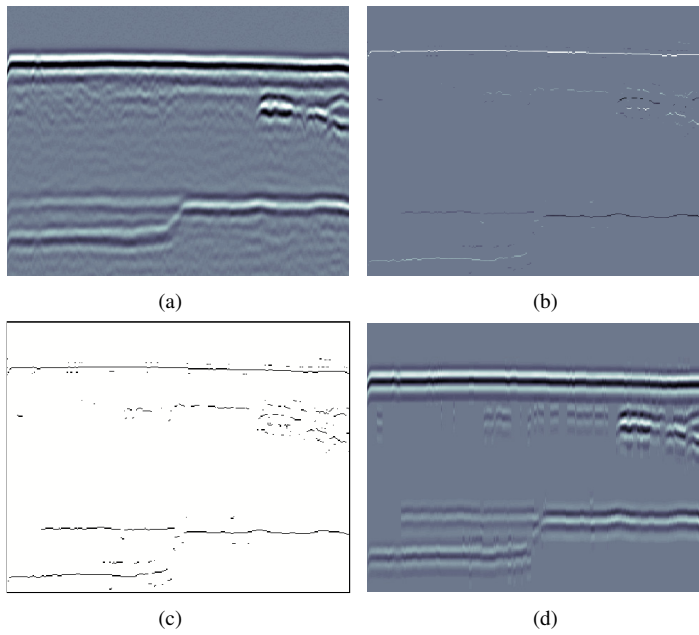


Fig. 11 (a): Original TOFD data ; (b): approximative solution of $\tilde{\mathbf{a}}$ with MP method in Section 3.2; (c): nonzero elements of the solution; (d): approximation of $\mathbf{s} \approx \mathbf{F} \cdot \tilde{\mathbf{a}}$.

In Figures 10(b) and 11(b), the results of the MP method (in Section 3.2) are shown. We obtain only very few nonzero values for each A-scan vector \mathbf{a} . Here in each column, we have taken in the first example (Figure 10(b)) at most $M = 10$ nonzero values, where M is the upper bound for the number of iterations of MP, and we have used the error bound $\varepsilon = 40$. For the example in Figure 11(b), $(M, \varepsilon) = (6, 60)$ has been taken. For a better illustration, Figures 10(c) and 11(c) show again the positions the nonzero coefficients, where “black” stands for nonzero and “white” for zero coefficients. Finally, the Figures 10(d) and 11(d) show an approximation of the TOFD data, where only the nonzero coefficients obtained by MP, are again convolved with the pulse function. Hence these representations can be seen as sparse approximations of the TOFD B-scans, and also yield a denoised image. However, most important for further investigation of possible flaws are the geometric data in (b) resp. (c).

In a third example we test the MP method for a back wall measurement. The B-scan of the back wall with scrap mark (Figure 12(a)) originates from a sample of a steel pipe of outer diameter 244.5 mm and wall thickness 13.8 mm. It has also been measured with the Omniscan iX system where we used a 4 MHz broadband transducer of 15 mm diameter (Karl Deutsch STS 15 WB 2-7) with nominal incidence angle. The resolution in scan direction is 0.5 mm and the sampling rate is 100 MHz with an 8-bit resolution. As before, we apply the MP method to each A-scan (each column) with at most $M = 5$ iterations and with $\varepsilon = 15$, where the MP procedure is

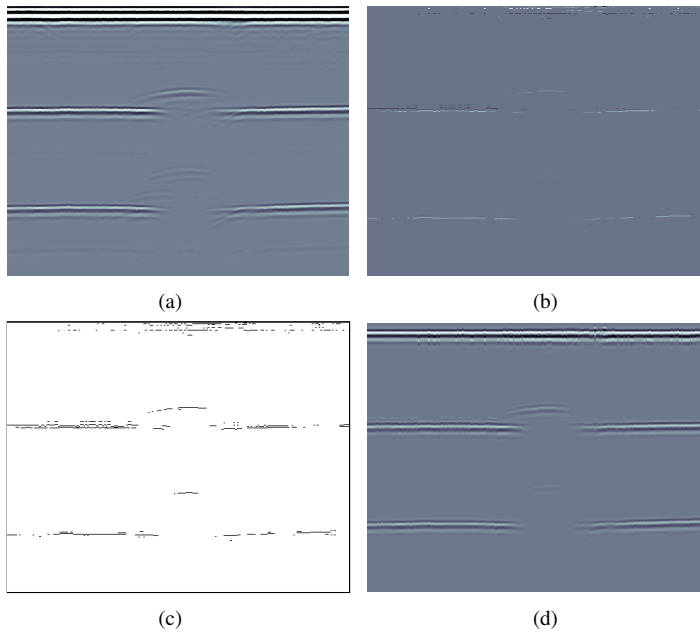


Fig. 12 (a): Original B-scan of a backwall; (b): approximate solution of \mathbf{a} with MP method; (c): nonzero elements of the solution; (d): approximation of $s \approx \mathbf{F} \cdot \mathbf{a}$.

stopped if the error does not exceed ε and (at latest) after M iterations. Figure 12(b) shows the nonzero coefficients of the \mathbf{a} vectors in each column. For a better illustration, the nonzero coefficients are black and the zero coefficients are white in Figure 12(c). Finally, Figure 12(d) shows the result of a convolution of the sparse matrix in (b) with the pulse yielding a sparse approximation (and a denoising) of the original data. At last, we remark that the used MP and OMP methods are suitable for real time computations. For the complete computation of all arrival times and amplitudes for data in Figures 10–12 together with the computation of the approximation of s in (d), our MATLAB MP algorithm using a 2.66 GHz Intel Core 2 Duo processor needs less than 0.1 seconds while the OMP requires 1 second for the data Figure 10 (data size 356×441), 0.9 seconds for Figure 11 (data size 356×331), and 0.65 seconds for Figure 12 (data size 636×201).

6.3 Simulations for parameter optimization

Finally, we want to illustrate the power of the proposed iterative Newton method for estimation of parameters in the pulse function model. For this purpose, we have used the following simulation. In a first step we have randomly chosen four amplitudes of different sizes in a vector of length 100. Further we have added some Gaussian noise to the vector (simulating microstructure noise) and have convolved the obtained vector with a Gabor function of type (2). The obtained A-scan simulation has been

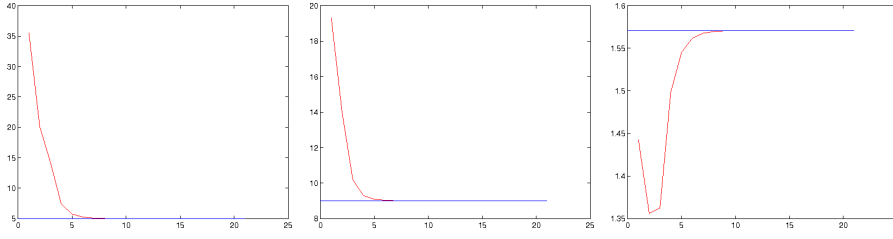


Fig. 13 Wave parameters (y-axis) against iteration steps (x-axis) (left α , middle ω , right ϕ), $\bar{\mathbf{a}}$ not noisy.

now processed as follows. We have taken an initial guess of a Gabor function with parameter vector θ_0 , and have applied the alternating algorithm (MP algorithm and iterative Newton method) as proposed in Section 2.

In our first example without noise, we started with $\theta_0 = (35, 19, 1.54)$ (α in $(MHZ)^2$ and ω in MHz) quite far away from the true parameter vector. The true parameters have been obtained already after 6 iterations of the method, namely $\theta = (5.0, 9.0, \pi/2)$, see Figure 13. Since there is no noise, we obtain a perfect approximation of the A-scan and therefore omitted the corresponding illustration.

In the second and third example, Gaussian noise of variance 0.01 has been used before convolving the vector with the Gabor function, this corresponds to the SNR 23.7. In Figure 14, the starting parameter vector is $\theta_0 = (12.5, 7.0, 1.2)$. Again we obtain a good estimate of the correct parameter vector $\theta = (5.0, 9.0, \pi/2)$ already after 6 iterations. The illustrations in the first row of Figure 14 show the parameters α , ω and ϕ after each iteration, the second row shows the approximation of the true Gabor function with the help of the found parameter vector and the approximation of the A-scan using 4 amplitudes found by the MP algorithm. Finally, in the last example a symmetric Gabor function has been used with $\theta = (5.0, 9.0, 0)$, while the starting vector has been taken $\theta_0 = (11.5, 7.7, 0.17)$. Again, the procedure approximately finds the correct parameters.

7 Conclusions and Outlook

The deconvolution methods presented in this work are supposed to be used as a pre-processing step for further applications. Our long term objective is to derive a method to invert the B-scans, see [21]. We would like to reconstruct the shape of the back wall based on the B-scan image. Usually, such inversion techniques provide better results if the raw data only contains low-level noise, and they tend to be unstable if the raw data is too noisy. Hence, it is important to apply a fast and effective denoising algorithm that is capable to preserve the important signal features while removing most of the noise.

In this paper, we have proposed two different deconvolution algorithms that both map an A-scan to a sparse vector that still contains the relevant information of the A-scan in an encoded form. This sparse representation of the A-scan resp. the B-scan can be differently processed:

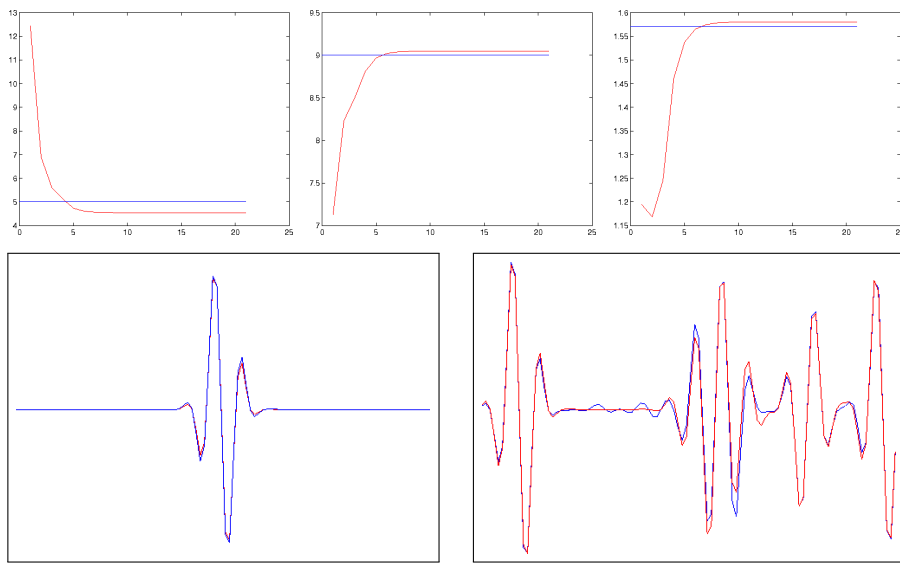


Fig. 14 Top: wave parameters after each iteration step (left α , middle ω , right ϕ); bottom: original (blue) and approximated (red) wave (left) and data (right); added Gaussian noise of variance 0.01 to $\bar{\mathbf{a}}$.

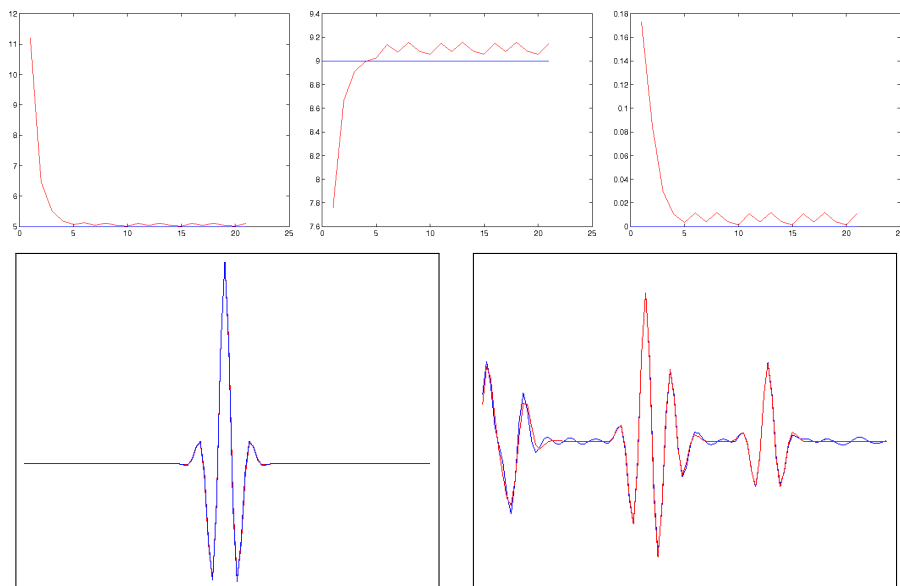


Fig. 15 Top: wave parameters after each iteration step (left α , middle ω , right ϕ); bottom: original (blue) and approximated (red) wave (left) and data (right), added Gaussian noise of variance 0.01 to $\bar{\mathbf{a}}$.

Flaw detection. A comparison of the significant coefficients in the sparse columns of the B-scan (after deconvolution) provides the positions of significant flaws in the material. Respectively, in the case of weld seam inspection, the sparse B-scan can be processed further by a direct inversion method, see [21]. Alternatively, a representation of the B-scan with only a few coefficients can be used for classification using machine-learning algorithms. The algorithm "learns" the B-scans corresponding to different classes (e.g. for different flaws in the back wall) and afterwards tries to assign the correct class to a new unknown B-scan. In such learning procedures, the algorithms are usually not able to handle full images but only a very limited number of representing attributes. Hence, the nonzero coefficients provided by our deconvolution algorithms will act as a good choice of representing attributes for such machine learning algorithms.

Denoising. A convolution of the obtained sparse vectors with the (computed or estimated) pulse echo yields a denoised B-scan. Since the deconvolution algorithms are suitably adapted to the measured signals (by using the transmitted pulse echo), this denoising method outperforms most direct (non-adaptive) denoising methods for images (see e.g. Figures 10-12).

Compression. Another advantage of our proposed algorithm is that the nonzero coefficients provide a strong compression of the B-scan. The whole B-scan is reduced to a small number of most significant coefficients, representing the relevant information. Knowing the shape of the pulse, it is possible to reconstruct the B-scan only with the knowledge of the position of the sparse nonzero coefficients. Apparently, this can be used to reduce the amount of storage significantly.

Acknowledgements We thank the referees and the editor for their valuable suggestions that led to a considerable improvement of the manuscript. This work is supported by the Central Innovation Programme SME (ZIM) of the Federal Ministry of Economics and Technology (BMWi). We also would like to thank Vallourec & Mannesmann Deutschland GmbH for their financial support.

References

1. S. Demirli, J. Saniie, Model-based estimation of ultrasonic echoes. Part I: Analysis and algorithms, *IEEE Trans. Ultrason. Ferroelect. Freq. Control* **48**(3):787–802 (2001).
2. K.F. Kaarensen, E. Bolviken, Blind deconvolution of ultrasonic traces accounting for pulse variance, *IEEE Trans. Ultrason. Ferroelect. Freq. Control* **46**(3):564–573 (1999).
3. J.M. Mendel, Optimal seismic deconvolution: An estimation-based approach, New York, Academic Press (1983).
4. A.T. Walden, Non-gaussian reflectivity, entropy, and deconvolution, *Geophysics* **50**(12):2862–2888 (1985).
5. H.-H. Ciang, C.L. Nikias, Adaptive deconvolution and identification of nonminimum phase FIR systems based on cumulants, *IEEE Trans. Automatic Contr.* **35**(1):36–47 (1990).
6. A.K. Nandi, D. Mämpel, B. Roscher, Comparative study of deconvolution algorithms with applications in non-destructive testing, *IEE Digest 145:1/1–1/6* (1995).
7. R. Neelamani, H. Choi, R. Baraniuk, ForWaRD: Fourier-wavelet regularized deconvolution for ill-conditioned systems, *IEEE Trans. Ultrason. Ferroelect. Freq. Control* **52**(2):418–432 (2004).
8. R.H. Herrera, R. Orozco, M. Rodriguez, Wavelet-based deconvolution of ultrasonic signals in non-destructive evaluation, *J. Zhejiang Univ. SCIENCE A* **7**(10):1748–1756 (2006).
9. T. Olofsson, Computationally efficient sparse deconvolution of B-scan images, in *Proc. IEEE Ultrason. Symp.*:540–543 (2005).

10. T. Olofsson, E. Wennerström, Sparse deconvolution of B-Scan Images, *IEEE Trans. Ultrason. Ferroelectr. Freq. Control* **54**(8):1634–1641 (2007).
11. S. Demirli, J. Saniie, Model-based estimation of ultrasonic echoes. Part II: Nondestructive Evaluation Applications, *IEEE Trans. Ultrason. Ferroelectr. Freq. Control* **48**(3):803–811 (2001).
12. I. Ziskind, M. Wax, Maximum likelihood localization of multiple sources by alternating projection, *IEEE Trans. Acoust. Speech Signal Processing* **36**(10):1553–1560 (1988).
13. C.F.J. Wu, On the convergence properties of the EM algorithm, *The Annals of Statistics* **11**(1):95–103 (1983).
14. P.J. Chung, J.F. Böhme, Comparative convergence analysis of EM and SAGE algorithms in DOA estimation, *IEEE Trans. Signal Process.* **49**(12):2940–2949 (2001).
15. S. Mallat, Z. Zhang, Matching pursuits with time-frequency dictionaries. *IEEE Trans. Signal Process.* **41**:3397–415 (1993).
16. J. Tropp, Greed is good: Algorithmic results for sparse approximation, *IEEE Trans. Inform. Theory* **50**:2231–2242 (2004).
17. T. Peter, D. Potts, M. Tasche, Nonlinear approximation by sums of exponentials and translates, *SIAM J. Sci. Comput.* **33**(4):1920–1944 (2011).
18. N. Ruiz-Reyes, P. Vera-Candeas, J. Curpián-Alonso, R. Mata-Campos, J.C. Cuevas-Martinez, New matching pursuit-based algorithm for SNR improvement in ultrasonic NDT, *NDT&E International* **38**:453–458 (2005).
19. N. Ruiz-Reyes, P. Vera-Candeas, J. Curpián-Alonso, J.C. Cuevas-Martinez, J.L. Blanco-Claraco, High-resolution pursuit for detecting flaw echoes close to the material surface in ultrasonic NDT, *NDT&E International* **39**:487–492 (2006).
20. E. Mor, A. Azoulay, A. Mayer, A matching pursuit method for approximate overlapping ultrasonic echoes, *IEEE Trans. Ultrason. Ferroelectr. Freq. Control* **57**(7):1996–2004 (2010).
21. F. Boßmann, Entwicklung einer automatisierten Auswertung von bildgebenden Ultraschallverfahren, diploma thesis, University of Duisburg-Essen, Germany, 2009.